J. Am. Soc. Mass Spectrom. (2018) 29:2125–2137
DOI: 10.1007/s13361-018-2047-2

RESEARCH ARTICLE

Modified Quadrupole Ion Trap Mass Spectrometer for Infrared Ion Spectroscopy: Application to Protonated Thiated Uridines

L. A. Hamlow,[1] Y. Zhu,[1] Zachary J. Devereaux,[1] N. A. Cunningham,[1] G. Berden,[2] J. Oomens,[2] M. T. Rodgers[1]

[1]Department of Chemistry, Wayne State University, 5101 Cass Ave., Detroit, MI 48202, USA
[2]Institute for Molecules and Materials, FELIX Laboratory, Radboud University, Toernooiveld 7c, 6525 ED, Nijmegen, The Netherlands

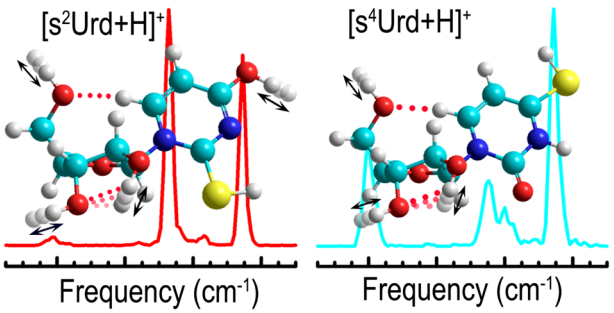

Abstract. Modifications to a Paul-type quadrupole ion trap mass spectrometer providing optical access to the trapped ion cloud as well as hardware and software for coupling to a table-top IR optical parametric oscillator laser (OPO) are detailed. Critical experimental parameters for infrared multiple photon dissociation (IRMPD) on this instrument are characterized. IRMPD action spectra, collected in the hydrogen-stretching region with this instrument, complemented by spectra in the IR fingerprint region acquired at the FELIX facility, are employed to characterize the structures of the protonated forms of 2-thiouridine, $[s^2Urd+H]^+$, and 4-thiouridine, $[s^4Urd+H]^+$. The measured spectra are compared with predicted linear IR spectra calculated at the B3LYP/6-311+G(d,p) level of theory to determine the conformers populated in the experiments. This comparison indicates that thiation at the 2- or 4-positions shifts the protonation preference between the 2,4-H tautomer and 4-protonation in opposite directions versus canonical uridine, which displays a roughly equal preference for the 2,4-H tautomer and O4 protonation. As found for canonical uridine, protonation leads to a mixture of conformers exhibiting C2′-*endo* and C3′-*endo* sugar puckering with an anti nucleobase orientation being populated for both 2- and 4-thiated uridine.

Keywords: Infrared multiple photon dissociation action spectroscopy, IRMPD, Quadrupole ion trap mass spectrometer, QIT MS, RNA modifications, 2-Thiouridine, 4-Thiouridine, Uridine

Received: 27 June 2018/Revised: 31 July 2018/Accepted: 1 August 2018/Published Online: 22 August 2018

Introduction

Infrared ion spectroscopy (IRIS), specifically infrared multiple photon dissociation (IRMPD) action spectroscopy, has become an important tool in the study of gas-phase ion structure in recent years [1–4]. The utility of this technique has historically been enabled only by intense, broadly-tunable free-electron lasers (FELs) present at just a few facilities across the globe [5–8]. Recently, table-top optical parametric oscillator laser (OPO) sources have become available that are able to provide complementary power to FELs in the hydrogen-stretching region and thus enable more widespread accessibility to the infrared spectrum of gas-phase ions for IRMPD. IR OPOs can enable collection of IRMPD action spectra in the hydrogen-stretching region from 2300 to 3800 cm^{-1} [9–11]. Single-photon techniques such as cold ion spectroscopy can extend the usable range of these OPOs into the IR fingerprint region from 600 to 2300 cm^{-1} [12–18]. A variety of mass spectrometers have been utilized for IRIS, ranging from custom-built instruments to commercial instruments providing

Electronic supplementary material The online version of this article (https://doi.org/10.1007/s13361-018-2047-2) contains supplementary material, which is available to authorized users.

Correspondence to: M. Rodgers; *e-mail:* mrodgers@chem.wayne.edu

optical access to the ion population [4, 6, 19–23]. Recent work by Martens et al. demonstrated modifications for coupling a Bruker amaZon 3D quadrupole ion trap mass spectrometer (QIT MS) with both FEL and OPO [24]. Previous studies by our group have demonstrated the complementary power of the hydrogen-stretching and IR fingerprint regions in the determination of the intrinsic structures accessed by the protonated and sodium cationized forms of the canonical DNA and RNA nucleosides by electrospray ionization (ESI) [25–35].

Deoxyribonucleic acid (DNA) is the carrier of genetic information, whereas ribonucleic acids (RNAs) play crucial roles in the transcription and translation of that information into proteins. RNA is heavily modified, and these modifications play critical but often not fully understood roles in the functions of RNA, particularly in transfer RNA (tRNA) [36, 37]. It has long been known that modifications are critical to anticodon-codon interactions in tRNA, notably in the 34-position, known as the wobble-base [38, 39]. In the wobble hypothesis proposed by Crick, unmodified uridine in the wobble position is thought to recognize adenosine, through hydrogen-bonding interactions with the N3H and C4=O atoms of uridine, and wobble to guanosine [38] through hydrogen-bonding interactions with the C2=O and N3H atoms. However, uridine commonly undergoes post-transcriptional modification at this position, altering its binding to the codon by changing the base pairing at the wobble base [40]. 2-Thiouridine (s^2Urd) is a well-known modified uridine found at the wobble position of certain tRNAs, thought to alter the wobble preference towards adenosine by providing a less effective hydrogen-bond acceptor, C2=S, to N1H of guanine [39–41]. Specifically, s^2Urd and its 5-substituted derivatives have been found in tRNAs for glutamic acid and lysine [39]. The structure of s^2Urd has been studied by NMR, crystallography, and theoretical studies, all of which indicate a strong preference for C3′-*endo* sugar puckering [42–44]. This strong preference is also thought to play a role in the wobble pairing of s^2Urd [44–47].

An important isomer of s^2Urd that is also found natively in some tRNAs, though plays a more notable role in some RNA analyses, is 4-thiouridine (s^4Urd) [48, 49]. s^4Urd is known to be photoactive in tRNA and is attributed to conferring some degree of protection from near-UV exposure by cross-linking with a nearby cytidine [49–51]. s^4Urd may be incorporated into RNA in place of uridine in a metabolic labeling procedure to then crosslink a biotin tag and identify recently transcribed RNAs by separation [52]. A similar process can also be used to examine RNA–protein binding by incorporating s^4Urd into RNA and UV cross-linking it to RNA-binding proteins [53]. The importance of these techniques in further understanding the roles of RNA within the cell and the development of complementary techniques in the mass spectrometer increases the desire to understand the intrinsic effects of thiation on the gas-phase structures of uridine [54–57].

The current work investigates the structures of the protonated forms of s^2Urd and s^4Urd, $[s^2Urd+H]^+$ and $[s^4Urd+H]^+$, accessed by ESI via IRMPD action spectroscopy using a Fourier transform ion cyclotron resonance mass spectrometry (FT-ICR MS) and QIT MS. These instruments were coupled to the FELIX FEL and a table-top OPO laser, respectively. The chemical structures of s^2Urd and s^4Urd are compared to that of canonical Urd in Figure 1. Electronic structure calculations were used to characterize stable structures of the protonated forms of these modified nucleosides, predict their linear IR spectra, and calculate their relative stabilities. Comparison of the measured IRMPD spectra with predicted linear IR spectra reveals the preferred protonation sites and the low-energy conformations accessed in these experiments. The measured spectra of $[s^2Urd+H]^+$ and $[s^4Urd+H]^+$ are also compared to that measured for $[Urd+H]^+$ [27] and those for the protonated forms of 2- and 4-thiouracil, $[s^2Ura+H]^+$ and $[s^4Ura+H]^+$ [58], respectively. These comparisons enable elucidation of the influence of the sugar and 2- and 4- thiation modifications of the nucleobase on the conformers accessed.

Experimental Description

Materials

s^2Urd and s^4Urd were purchased from Carbosynth (San Diego, CA, USA). The HPLC-grade methanol, water, and trifluoroacetic acid used during experiments in the IR fingerprint region were purchased from Sigma Aldrich (Zwijndrecht, The Netherlands). The HPLC-grade methanol and glacial acetic acid used in experiments in the hydrogen-stretching region were purchased from Fischer Scientific (Waltham, MA, USA), and the HPLC-grade water used in these experiments was purchased from Sigma Aldrich (St. Louis, MO, USA).

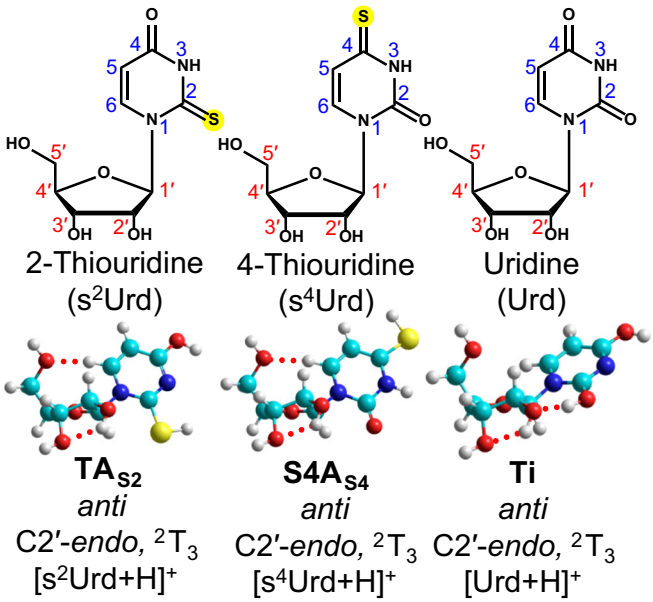

Figure 1. Structures of neutral 2-thiouridine, 4-thiouridine, and canonical uridine with atom numbering of the nucleobase and sugar shown. Ground conformers of $[s^2Urd+H]^+$, $[s^4Urd+H]^+$, and $[Urd+H]^+$ predicted at B3LYP/6-311+G(2d,2p)//B3LYP/6-311+G(d,p) level of theory. Site of protonation, sugar puckering, and nucleobase orientation are indicated

Modified Bruker amaZon ETD QIT MS

Figure 2 displays a schematic of the amaZon ETD QIT MS (Bruker, Billerica, MA, USA) described subsequently. Ions are generated in an ESI source consisting of a pneumatic nebulizer and enclosed spray chamber. Typically, solutions containing micromolar concentrations of the relevant analyte are introduced via a syringe pump at 1.6–3 μL/min to the nebulizer, which uses pressurized N_2 to pneumatically assist spray generation. In this work, 25 μM solutions of s^2Urd or s^4Urd in 50:50 methanol/water were introduced at 3 μL/min. Heated N_2 gas flows counter to the direction of ion flow, assisting in desolvation and rejection of neutrals from the inlet of the mass spectrometer. The nebulizer assembly is held at ground potential against a glass capillary with a metal-coated entrance that is held at −3 to −5 kV for positive ions and 250–500 V below the spray shield voltage directly in front of the capillary entrance (−4.5 kV and 500 V in this work). Ions and charged droplets are focused onto the capillary entrance, where they are carried into the instrument by the flow of gas from the spray chamber to the first vacuum stage. The capillary exit is metal coated and held at 50–200 V (140 V in this work). The capillary is offset from the axis of the instrument and exits into the first of two radio frequency (RF) ion funnels that collect and transmit ions, while helping to reject neutrals, and thus reducing contamination of downstream optics. A DC lens between the ion funnels can be used for in-source activation via collision-induced dissociation (CID), or the DC potentials on the ion funnel can be tuned to produce collisional cooling conditions. Ions exit the second ion funnel into an octopole ion guide, which guides the ions to an assembly of gates and focusing lenses from which they can enter the quadrupole ion trap.

A typical MS/MS sequence for this instrument begins with clearing the trap of ions from the previous scan by turning off the RF voltage applied to the ring electrode. The primary RF is then turned back on, and ions are accumulated in the trap for 0.5–50 ms by lowering the gate voltage before the first end cap electrode. Ions are trapped by the primary RF field, which is a nearly quadrupolar 781 kHz RF field of 400–800 $V_{p\text{-}p}$, and are collisionally cooled to the center of the trap by ~10^{-3} Torr helium. The ions of interest are isolated using with an auxiliary RF field applied between the end cap electrodes. Delays can be added before and after ion isolation to collisionally cool the ions and circumvent undesired collisional heating during the isolation step. CID is performed by exciting the trapped ions with the auxiliary RF field during an activation segment. A TTL signal corresponding to the activation segment is output from the instrument for use by external devices. An excitation window with no auxiliary RF amplitude is used to signal this segment to the laser system for IRMPD experiments. Multiple stages of ion activation can be coupled together with the appropriate isolation steps and delays to perform MS^n experiments. Different ion activation methods can be used allowing for collection of IRMPD action spectra of product ions generated by CID, electron transfer dissociation (ETD), or photodissociation with a CO_2 laser [24]. Ions are then excited out of the trap to a conversion dynode detector for mass analysis and detection.

A crucial physical modification was made to the QIT MS to enable optical access to the trapped ions. The original ring electrode was replaced by a modified ring electrode with two 2 mm holes drilled through the center of the top and bottom of the ring electrode. Two 1 in. outer diameter IR transparent windows (BaF_2, Thorlabs, Newton, NJ, USA) were mounted on a modified flange to the high vacuum region in which the QIT is located. A set of M6x1 holes on a 25 mm grid were also incorporated into this flange to facilitate mounting of optical components above the QIT MS. Two ½ in. gold-coated mirrors (Thorlabs) were mounted in a custom mirror mount (Bruker), which positions them below the trap assembly. These mirrors redirect the laser beam passing through the trap out of the instrument where it can be directed to a beam dump. After recalibration of the instrument, no reduction in performance

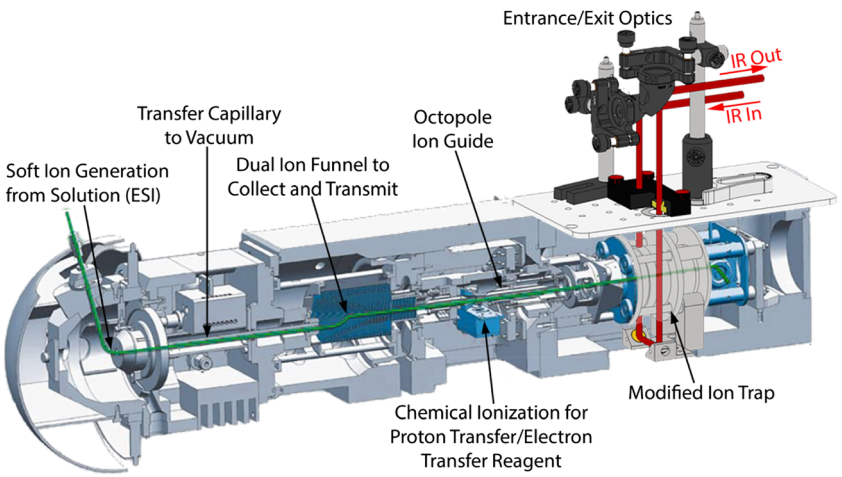

Figure 2. Schematic overview of the modified amaZon ETD quadrupole ion trap mass spectrometer and electrospray ionization source. The flange to the high-vacuum region has been replaced with a small optical breadboard having two BaF_2 windows for passage of the laser beam into and out of the vacuum region. The ion trap has been modified with a 2 mm hole machined through the ring electrode, oriented vertically in the instrument. Mirror mounts have been installed to guide the beam into and out of the vacuum region

was observed with respect to isolation, fragmentation, or resolution relative to the performance observed prior to this modification.

IRMPD Action Spectroscopy in the Hydrogen-Stretching Region

The modified amaZon ETD QIT MS is coupled to an OPO (LaserVision, Bellevue, WA, USA) pumped by the 1064 nm fundamental line of a pulsed Nd:YAG (Continuum Lasers, San Jose, CA, USA). This system readily generates mid-IR photons in the range of 2.1–5 μm (1970–4690 cm^{-1}), with a bandwidth of ~ 3–4 cm^{-1}, in 7 ns pulses of 5–18 mJ at a 10 Hz repetition rate. The mid-IR output from the OPO immediately enters an enclosure flushed with dry N_2 gas to minimize IR absorption by ambient water vapor. Upon entering this enclosure, an optical shutter (SH05, Thorlabs), triggered to open by the activation segment TTL signal described in the previous section, intersects the beam. During the activation segment, the beam passes through the enclosure and is focused into the ion trap, approximately to the center of the ion cloud, interacting with any trapped ions. To ensure that every activation segment contains the same number of laser pulses, an active-low TTL signal associated with the Nd:YAG flashlamp discharge, about 100 ns offset from the laser output, is converted to active-high by a delay generator (Model 505, Berkeley Nucleonics Corp., San Rafael, CA, USA) and sent to the auxiliary input of the QIT MS where it is used to trigger the start of each MS/MS sequence. The activation segment and Nd:YAG flashlamp signals are monitored on a digital oscilloscope for verification of the activation segment length and consistency in the number of pulses within.

The IR output of the OPO is controlled and monitored using LabView subVIs supplied with the system. These subVIs, i.e., the laser frequency, are commanded by and synchronized to the QIT MS by a custom LabView program. The OPO is scanned through a series of specified output frequencies, typically in increments near the laser bandwidth (3–4 cm^{-1}). At each of these points, data collection is paused until the QIT MS receives a software trigger through its XML interface [24], which is accessible in service mode of the TrapControl software. This trigger is sent after the OPO has finished changing its output to the appropriate frequency and includes frequency information for the data file as well as the command to begin collecting the next spectrum upon arrival of the next trigger from the Nd:YAG. A single mass spectrum is recorded at prescribed wavelengths, typically consisting of 5–10 averaged MS/MS sequences.

IRMPD spectra for $[s^2Urd+H]^+$ and $[s^4Urd+H]^+$ were collected on this instrument, with irradiation for 2.0 and 1.5 s respectively, between 3300 and 3800 cm^{-1}. Wavelengths, reactant and product ion intensities, and IRMPD yields are output to a text file by a Visual Basic script in DataAnalysis 4.2 (Bruker Daltonics) for further analysis. Photodissociation of $[s^2Urd+H]^+$ and $[s^4Urd+H]^+$ results in cleavage of the N-glycosidic bond and production of the protonated nucleobase, $[s^2Ura+H]^+$ and $[s^4Ura+H]^+$, respectively. The IRMPD yields were calculated from the reactant and product ion intensities as shown in Eq. (1).

$$\text{IRMPD yield} = \sum_i I_{\text{product}_i} \Big/ \left(I_{[\text{Nuo+H}]^+} + \sum_i I_{\text{product}_i} \right) \quad (1)$$

The IRMPD yield in the hydrogen-stretching region was not corrected for frequency-dependent power as the power output of the OPO was roughly constant across the range examined.

IRMPD Action Spectroscopy in the IR Fingerprint Region

IRMPD action spectra in the IR fingerprint region were measured for $[s^4Urd+H]^+$ and $[s^2Urd+H]^+$ using a custom-built 4.7 T Fourier-transform ion cyclotron resonance mass spectrometer (FT-ICR MS) [59, 60] coupled to the FELIX free electron laser (FEL) [61]. s^2Urd and s^4Urd were diluted to 1.5 mM in 50:50 methanol:water with 10 mM trifluoroacetic acid. The protonated species were generated by electrospray ionization (ESI) using a Micromass "Z-spray" source with a solution flow of 7 μL/min. Ions were collected, trapped, and thermalized in a hexapole ion guide before being extracted through a quadrupole bender and transferred into the ICR cell by an octopole ion guide. The $[s^2Urd+H]^+$ and $[s^4Urd+H]^+$ ions of interest were isolated using a SWIFT pulse and excited by IR photons in the range of 700 to 1900 cm^{-1} from the FEL for 2.0 and 1.5 s, respectively. The IRMPD yield in the IR fingerprint region was linearly corrected for the frequency dependent variation of the FEL pulse energy.

Computational Methods

Previous studies published on the interpretation of IRMPD spectra of protonated uridine $[Urd+H]^+$, 2′-deoxyuridine $[dUrd+H]^+$ [22], and protonated uracil $[Ura+H]^+$ [58] indicated that protonation at the 4- and 2-positions as well as the 2,4-dihydroxy tautomer were likely candidates for protonation. The protonated nucleobases corresponding to the nucleosides studied here, $[s^2Ura+H]^+$ and $[s^4Ura+H]^+$ [58], also found that protonation at the 4- and 2-positions as well as the 2,4-sulfhydryl-hydroxyl, and 2,4-hydroxy-sulfhydryl tautomers were most likely, and therefore, each of these protonation sites was examined here. Candidate structures for each protonation site were generated by a simulated annealing procedure using HyperChem 8.0 with the Amber 3 force field. In every cycle of simulated annealing, the temperature of the system was ramped from 0 to 1000 K over 0.2 ps, held at 1000 K for 0.3 ps allowing the structure to explore conformational space, and then cooled back to 0 K over 0.2 ps, with an optimization step to relax the structure to a local minimum. For each protonated form, 300 consecutive cycles were used to generate 300 low-energy candidate structures. The 40 most stable structures for each protonated form found via simulated annealing, along with suitably modified structures analogous to those found in prior work for $[Urd+H]^+$ [27] were included to

comprehensively sample conformational space. The Gaussian 09 suite of programs was used to perform geometry optimizations, frequency analyses, and single-point energy determinations [62]. All candidate structures were optimized using the B3LYP density functional theory (DFT) method with the 6-311+G(d,p) basis set, which was also used to perform frequency analyses of the optimized structures. Single-point energy calculations were performed at the B3LYP and MP2(full) levels of theory with the 6-311+G(2d,2p) basis set. These levels of theory and basis sets have been found in previous studies to predict spectra in good agreement with measured IRMPD spectra [26, 27, 30–32, 63], and relative energetics in good agreement with those in the experiment [63–69].

The calculated vibrational frequencies for $[s^2Urd+H]^+$ and $[s^4Urd+H]^+$ were scaled by factors of 0.977 and 0.975 in the IR fingerprint region, and 0.954 and 0.956 in the hydrogen-stretching region, respectively, for comparison to the experiments. In the IR fingerprint region, the vibrational frequencies were convoluted with a 20-cm^{-1} full-width-at-half-maximum (FWHM) Gaussian line shape and a 15-cm^{-1} FWHM Gaussian line shape in the hydrogen-stretching region. The harmonic approximation for vibrations calculated with these methods cannot fully represent the anharmonic nature of real systems. System-dependent anharmonicity can affect both the observed frequencies, by not accounting for anharmonic motion, and the relative band intensities, due to anharmonic coupling to nearby vibrational modes. Therefore, some inconsistencies between the measured IRMPD spectrum and calculated linear IR spectrum are expected. Disagreements are generally limited enough that the measured IMRPD spectrum is well-represented by the linear IR spectrum [9].

Safety Considerations

Intense light is produced across the visible, near-IR, and mid-IR wavelength ranges. Appropriate laser safety eyewear should be worn at all times near any exposed beams, in particular the 1064 nm Nd:YAG used to pump the OPO, which is invisible to the naked eye. Care should be taken to prevent any flammable materials being present near the focal point of the IR beam.

Results

IRMPD Action Spectroscopy

IRMPD action spectra of $[s^2Urd+H]^+$ and $[s^4Urd+H]^+$ are compared in Figure 3. While these ions are isomeric and impossible to differentiate with MS alone, IRMPD action spectroscopy readily distinguishes these species. Perhaps the most obvious deviation between the spectra of these isomeric nucleosides is the intense peak at 1785 cm^{-1} in the spectrum of $[s^4Urd+H]^+$, a feature not observed for $[s^2Urd+H]^+$. The region between 1000 and 1500 cm^{-1} also displays a number of notably obvious differences in the measured spectra. In the hydrogen-stretching region, many of the frequencies observed for these isomeric nucleosides are similar, but significant disparity is seen in the relative intensities. Similar disparities in the relative intensities can also be seen in the features between 1550 and 1650 cm^{-1}.

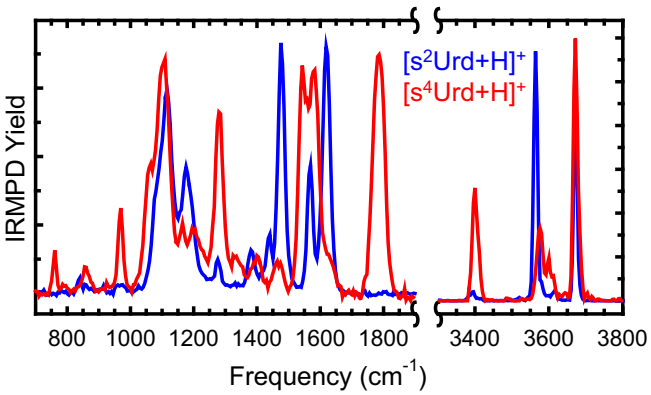

Figure 3. Experimental IRMPD action spectra of $[s^2Urd+H]^+$ and $[s^4Urd+H]^+$ over the IR fingerprint and hydrogen-stretching regions

Performance of Modified QIT MS for IRMPD Action Spectroscopy

Several primary figures-of-merit for IRMPD in the QIT MS are the neutral gas pressure, laser power, laser irradiation time, and laser overlap with the ion cloud. The helium gas pressure within the trap is regulated through the primary gas controller (GC_{He}), which can be used to provide 0 to 100% gas flow through a proportional valve. Typically, GC_{He} values of ~ 20% correspond to an increase in background pressure of 0.75×10^{-6} Torr vs. no He. To examine the effects of this pressure on IRMPD yield, spectra of protonated tryptophan (a well-characterized system [24, 70]) were collected while varying GC_{He} from 5 to 80% (Figure 4). Reduced collisional cooling at low pressures resulted in higher dissociation yields, but reduced trapping efficiency, and led to greater noise. As pressure in the trap increased, the IRMPD yield decreased in concert with the noise, though not linearly across the pressure range. A pressure-dependent balance of IRMPD yield and noise was found for GC_{He} values of ~ 25% for this QIT MS instrument. Ion intensity also plays an important role in determining the signal-to-noise ratio of the IRMPD yield and can be improved by increasing GC_{He} up to a limit after which ion intensities may decrease. It is important to note that the very small feature observed in Figure 4 around 3300 cm^{-1} was still observable until around 60% GC_{He} and decreases very little from ~ 20% GC_{He}. Below ~ 20% GC_{He}, the size of this small feature is comparable to the noise making it difficult to distinguish. Likewise, at $GC_{He} > 60\%$, the feature around 3300 cm^{-1} is small enough to be indistinguishable from the noise.

Figure 5 displays a series of IRMPD spectra of $[s^2Urd+H]^+$ in the hydrogen-stretching region collected at different laser powers and irradiation times that demonstrate the importance of tuning the energy available for dissociation. Operating at full laser power resulted in saturation of the two most intense

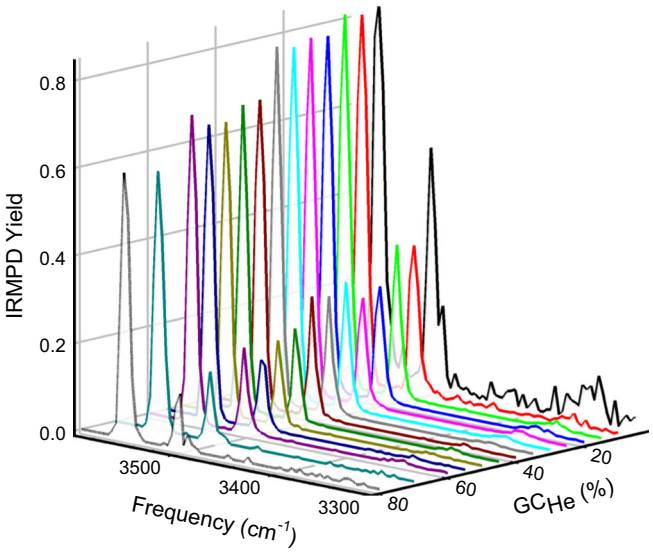

Figure 4. IRMPD action spectra of $[Trp+H]^+$ in the hydrogen-stretching region at a series of He pressures within the ion trap, controlled by the built-in He valve (GC_{He}) set from 5 to 80%. Laser power was detuned to roughly half of the maximum power to prevent saturation of the spectral features above 3500 cm^{-1}. Ions were irradiated for 0.5 s. The data represent averages of 10 MS/MS scan sequences

features and significant broadening of all features. Decreasing the irradiation time and laser power until the most intense peak has ~ 50% IRMPD yield results in even more substantial peak narrowing, increases the signal-to-noise ratio, and results in more robust relative intensities. In the current work, reduction of the OPO power from 127 to 60 mW at 3500 cm^{-1} enabled acquisition of spectra exhibiting much narrower features, while also reducing peak saturation and retaining the less intense features observed at higher power.

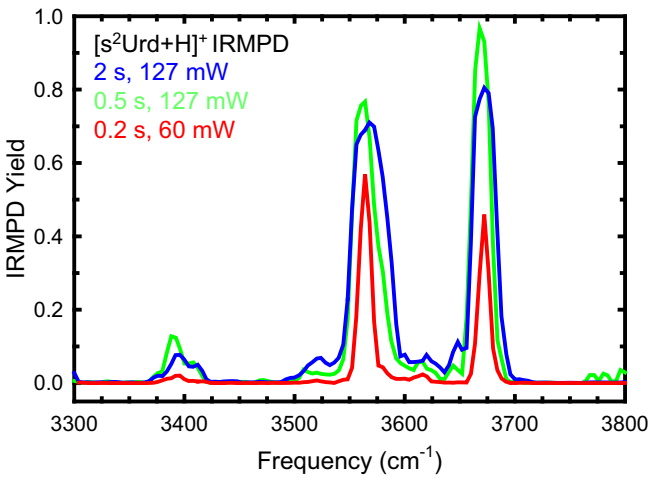

Figure 5. IRMPD action spectra in the hydrogen-stretching region of $[s^2Urd+H]^+$ acquired at different irradiation times and laser powers. The measured feature widths, relative intensities, and noise demonstrate the importance of choosing appropriate conditions in obtaining high quality, reproducible spectra that minimize analysis uncertainty

Theoretical Results

Relative B3LYP and MP2 Gibbs free energies (ΔG_{298}) as well as important structural parameters for select low-energy structures representing unique structures and each protonation site determined for $[s^2Urd+H]^+$ and $[s^4Urd+H]^+$ are compared in Table 1. Structural characteristics and energetics of all low-energy structures within ~ 25 kJ/mol of the ground conformers and representing unique structures and each protonation state are listed in Table S1 of the Electronic Supplementary Information; images of these structures can be seen in Figures S1 and S2. The nomenclature used to label these structures is based on the protonation site/tautomeric conformation, T for the 2-hydroxy-4-sulfhydryl or 2-sulfhydryl-4-hydroxy tautomers, or O2, S2, O4, or S4 for the protonated canonical species. This designation is followed by a capital letter indicating relative stability alphabetically within the family of conformers for that protonation site based upon the calculated B3LYP 298 K Gibbs free energies. Finally, a subscript S2 or S4 is used to distinguish conformers of $[s^2Urd+H]^+$ or $[s^4Urd+H]^+$, respectively. The major structural features of interest in this work are the sugar ring puckering, nucleobase orientation with respect to the sugar, and theoretical base-pairing interaction. Sugar puckering is commonly described by the single ring atom lying outside of the plane of the ring, e.g., C2′-*endo* (where the C2′ atom lies above, *endo*, the plane defined by the other four atoms in the ring). A more specific description of this puckering that retains use of these well-known names was put forth by Altona and Sundaralingam [71] as a pseudorotation angle (P) and was calculated for every computed structure in this work. This pseudorotation angle along with the ∠C1′C2′C3′C4′ sugar ring dihedral angle used to calculate P is used to assign a specific envelope (E) or twisted (T) pucker. The atoms puckered above or below the plane of the sugar ring are indicated by the corresponding atom number superscripted or subscripted by the E/T designator, respectively (e.g., C2′-*endo* → ^{2}E). For twisted structures, major puckered atoms are listed to the left of the E/T designator, whereas minor puckered atoms are indicated to the right (e.g., $^2T_3$). The common descriptions, such as C2′-*endo*, apply specifically to corresponding envelope structures (e.g., ^{2}E), but nearby twisted conformers such as $^2T_1$ and $^2T_3$ are also described as C2′-*endo* as they are difficult to visually distinguish. No calculated structures in this work displayed ideal envelope structures; therefore, all further references to the common descriptions refer to a twisted description with a pseudorotation angle within 18° of the corresponding envelope structure (e.g., C2′-*endo*, ^{2}E, 162° or C3′-*endo*, ^{3}E, 18°). Nucleobase orientation is described as either *anti* or *syn* where the nucleobase orientation facilitates Watson-Crick [38] or Hoogsteen [72] base pairing, respectively. However, these two identifications must describe the full rotation of the nucleobase around the glycosidic bond. Therefore, the glycosidic bond dihedral angle, ∠O4′C1′N1C2, is also calculated and used to further describe nucleobase orientation as necessary. Many of the lowest energy-optimized structures

Table 1. Relative Free Energies of Stable Low-energy Conformers of $[s^2Urd+H]^+$ and $[s^4Urd+H]^+$ that Represent Each Unique Protonation Site and Those Structures that Exhibit Good Spectral Matching to the Experimental IRMPD Spectrum[a]

Species	Conformer	ΔG_{298} B3LYP	ΔG_{298} MP2	P (°)	Nucleobase orientation	Sugar puckering
$[s^2Urd+H]^+$	$\mathbf{TA_{S2}}$	0.0	0.0	164.9	*anti*	C2′-*endo* ($^2T_3$)
	$\mathbf{TB_{S2}}$	2.9	2.4	19.4	*anti*	C3′-*endo* ($^3T_4$)
	$\mathbf{TC_{S2}}$	4.1	2.4	167.5	*anti*	C2′-*endo* ($^2T_3$)
	$\mathbf{TD_{S2}}$	6.0	5.7	169.2	*anti*	C2′-*endo* ($^2T_3$)
	$\mathbf{S2A_{S2}}$	21.4	20.6	169.2	*anti*	C2′-*endo* ($^2T_3$)
	$\mathbf{O4B_{S2}}$	25.0	25.3	16.6	*anti*	C3′-*endo* ($^3T_2$)
	$\mathbf{O4C_{S2}}$	25.6	28.0	163.8	*anti*	C2′-*endo* ($^2T_3$)
$[s^4Urd+H]^+$	$\mathbf{S4A_{S4}}$	0.0	1.0	165.6	*anti*	C2′-*endo* ($^2T_3$)
	$\mathbf{S4B_{S4}}$	0.5	1.1	12.5	*anti*	C3′-*endo* ($^3T_2$)
	$\mathbf{TA_{S4}}$	5.9	0.0	165.2	*anti*	C2′-*endo* ($^2T_3$)
	$\mathbf{O2A_{S4}}$	26.2	17.2	169.5	*anti*	C2′-*endo* ($^3T_3$)

[a]Structures and frequencies were calculated at the B3LYP/6-311+G(d,p) level of theory. Gibbs free energies were calculated at the B3LYP/6-311+G(2d,2p) and MP2(full)/6-311+G(2d,2p) levels at 298 K and are given in kJ/mol. The pseudorotation angle, nucleobase orientation, and sugar puckering for each structure are also listed

exhibit C2′-*endo* or C3′-*endo* sugar puckering, although several alternate sugar puckering conformations are found among the stable structures computed, such as C1′-*exo*, C4′-*exo*, O4′-*exo*, and C3′-*exo*. However, conformers exhibiting these less common sugar puckerings typically lie higher in free energy. Images of specific structures discussed in greater detail subsequently can be found in Figures S1 and S2 of the Electronic Supplementary Information.

Hydroxyl-Sulfhydryl Tautomers

2-Sulfhydryl-4-hydroxyl tautomers are the only structures found below 20 kJ/mol by both B3LYP and MP2 for $[s^2Urd+H]^+$. The most stable calculated 2-sulfhydryl-4-hydroxyl tautomers of $[s^2Urd+H]^+$, $\mathbf{TA_{S2}}$ and $\mathbf{TB_{S2}}$, adopt an *anti* nucleobase orientation. $\mathbf{TA_{S2}}$ and $\mathbf{TB_{S2}}$ display C2′-*endo* and C3′-*endo* sugar puckering, respectively, and are stabilized by O2′H···O3′ intramolecular hydrogen-bonding interactions in their sugars. A C6H···O5′ noncanonical hydrogen bond between the nucleobase and sugar stabilizes their *anti* nucleobase orientation. $\mathbf{TB_{S2}}$ is calculated to be just 2.9 kJ/mol (B3LYP) and 2.4 kJ/mol (MP2) higher in free energy than $\mathbf{TA_{S2}}$. $\mathbf{TC_{S2}}$ is parallel to $\mathbf{TA_{S2}}$ in its C2′-*endo* sugar puckering and C6H···C5′ hydrogen bonding, but it lies 4.1 kJ/mol (B3LYP) and 2.4 kJ/mol (MP2) higher in Gibbs energy due to the inversion of the sugar hydrogen-bonding interaction to O3′H···O2′. $\mathbf{TD_{S2}}$ is calculated to be 6.0 kJ/mol (B3LYP) and 5.7 kJ/mol (MP2) less stable than $\mathbf{TA_{S2}}$ and adopts a C2′-*endo*, *anti* structure while displaying a S2H···O2′H···O3′ dual hydrogen-bonding interaction. The most stable *syn* structures found for $[s^2Urd+H]^+$, $\mathbf{TI_{S2}}$ and $\mathbf{TJ_{S2}}$, lie 17–18 kJ/mol higher in energy than $\mathbf{TA_{S2}}$ with $\mathbf{TJ_{S2}}$ displaying a S2···HO5′ hydrogen bond. The change in hydrogen bonding between these conformers can be explained by the increased bond length of S2–H over O2–H providing less stability through the S2H···O5′ hydrogen bond in $\mathbf{TJ_{S2}}$ due to increased strain in the sugar ring.

Several 2-hydroxyl-4-sulfhydryl tautomers are found within 20 kJ/mol, while not calculated to be the ground conformer by B3LYP, MP2 predicts a tautomer ground conformer. The most stable tautomer of $[s^4Urd+H]^+$, $\mathbf{TA_{S4}}$, is highly parallel to $\mathbf{TA_{S2}}$, displaying C2′-*endo* sugar puckering, an *anti* nucleobase, and the same hydrogen-bonding interactions. $\mathbf{TB_{S4}}$ displays a similar O2H···O2′H···O3′ dual hydrogen-bonding interaction to $\mathbf{TD_{S2}}$, but it is found only 8.1 kJ/mol (B3LYP) and 2.2 kJ/mol (MP2) higher in free energy than $\mathbf{TA_{S4}}$. For $[s^4Urd+H]^+$, the lowest energy hydroxyl-sulfhydryl tautomer adopting a *syn* conformation, $\mathbf{TE_{S4}}$, lies only 5–6 kJ/mol higher in free energy than $\mathbf{TA_{S4}}$ and displays an O2H···O5′ hydrogen bond.

Protonation at the 4-Position

Conformers protonated at the 4-position lie relatively high in energy for $[s^2Urd+H]^+$ but display a thioamide group not present in the sulfhydryl-hydroxyl tautomers. The most stable O4-protonated conformers of $[s^2Urd+H]^+$, $\mathbf{O4A_{S2}}$, $\mathbf{O4B_{S2}}$, and $\mathbf{O4C_{S2}}$ display a mixture of C2′-*endo* and C3′-*endo* sugar puckering with *anti* nucleobase orientations. These conformers are calculated to lie within 1.5 kJ/mol (B3LYP) and 3.1 kJ/mol (MP2) of each other, but they are 23.9 kJ/mol (B3LYP) and 24.9 kJ/mol (MP2) less stable than the ground $\mathbf{TA_{S2}}$ conformer and differ by the hydrogen-bonding interaction between O2′ and O3′. The 4-hydroxyl hydrogen atom points away from N3 in all three structures. Rotation of this protonated hydroxyl substituent produces structures 10–12 kJ/mol higher in free energy than $\mathbf{O4A_{S2}}$. The lowest energy O4 conformer of $[s^2Urd+H]^+$ exhibiting a *syn* nucleobase, lies over 37.1 kJ/mol higher in free energy than $\mathbf{O4A_{S2}}$.

S4-protonated conformers are calculated by B3LYP to be the most stable conformers of $[s^4Urd+H]^+$. Eight low-energy S4 conformers were calculated within 5 kJ/mol by both B3LYP and MP2, $\mathbf{S4A_{S4}}$–$\mathbf{S4H_{S4}}$. Six of these conformers display *anti* nucleobase orientations and a mixture of C2′-*endo* and C3′-*endo* sugar puckering, and otherwise differ in intramolecular hydrogen bonding in the sugar and rotation of the S4-sulfhydryl moiety. Of the low-energy conformers, $\mathbf{S4F_{S4}}$ and $\mathbf{S4H_{S4}}$ are noteworthy due to the presence of the dual hydrogen-bonding interaction O3′H···O2′H···O2 and their C3′-*exo* sugar puckering. The most stable S4 protonated *syn* conformer of $[s^4Urd+H]^+$, $\mathbf{S4M_{S4}}$, lies 18.2 kJ/mol (B3LYP) and 33.2 kJ/mol (MP2) higher in free energy than the most stable S4 conformers, $\mathbf{S4A_{S4}}$ (B3LYP) and $\mathbf{S4F_{S4}}$ (MP2).

Protonation at the 2-Position

The lowest energy S2 and O2 protonated structures calculated for $[s^2Urd+H]^+$ and $[s^4Urd+H]^+$, **S2A$_{S2}$** and **O2A$_{S4}$** both display C2′-*endo* sugar puckering with *anti* nucleobase orientations and S2H···O2′H···O3′ and O2H···O2′H···O3′ dual hydrogen-bonding interactions, respectively, providing stability through an ion-dipole interaction, although both are calculated to be more than 20 kJ/mol (B3LYP) and 17 kJ/mol (MP2) less stable than the calculated ground conformers. This ion-dipole interaction also stabilizes the *syn* **O2B$_{S4}$** structure of $[s^4Urd+H]^+$, with an O2H···O5′ hydrogen bond, which is found to be only 0.4 kJ/mol (B3LYP) less stable and 0.1 kJ/mol (MP2) more stable than **O2A$_{S4}$**. The longer S–H bond found in the parallel S2 conformer **S2B$_{S2}$** results in a more strained sugar puckering parallel to **TJ$_{S2}$** and is a further 10.2 kJ/mol (B3LYP) less stable than **S2A$_{S2}$**. Higher-energy S2 protonated conformers of $[s^2Urd+H]^+$ found within 18.5 kJ/mol (B3LYP) of **S2A$_{S2}$** display similar variability in sugar puckering and hydrogen bonding as found for the T conformers. For $[s^4Urd+H]^+$ however, structures without the ion-dipole interactions of **O2A$_{S4}$** and **O2B$_{S4}$** lie ≥ 33.9 kJ/mol higher in free energy and exhibit a mixture of C2′-*endo* and C3′-*endo* puckering similar to that seen for $[s^2Urd+H]^+$.

Discussion

IRMPD Performance on the QIT MS

As described previously, the Bruker amaZon ETD QIT MS utilizes a helium buffer gas, typically at pressures on the order of 10^{-3} Torr within the confines of the trapping volume. Collisions with helium cool the kinetic energy of the ions but can also cool the internal energy of the ions in direct competition with the heating process of IRMPD. Therefore, understanding the effects of pressure and therefore collisional cooling on the measured IRMPD spectra is of particular importance to the collection of high quality data. Operation of the QIT MS at ~20% GC_{HE} corresponds well to the built-in "Maximum Resolution" mode of this instrument and performs well for IRMPD, which makes adjusting the instrument into a mode suitable for IRMPD more robust. For systems such as protonated tryptophan that undergo very facile dissociation, where there may be notable fragmentation of the reactant ion prior to irradiation, increasing the He pressure beyond ~20% was helpful to increase collisional cooling. For systems where IRMPD is less efficient, slightly decreasing the He pressure in the trap was found to enhance the IRMPD yield, but at a cost of increased noise. While helium pressure in the trap certainly affects the resultant IRMPD action spectrum, there appears to be a reasonably wide range of pressures over which its effects are subtle. Small features remained distinguishable as pressure was increased until approximately 60% GC_{He}, while noise is reduced to a greater degree until about 50% GC_{He}.

Laser power and irradiation time were found to have a greater effect on the IRMPD spectrum acquired, while also being more straightforward to tune. The available power from the OPO used here was more than sufficient for collection of spectra over the hydrogen-stretching region of the protonated thiated uridines examined in this work, resulting in substantial saturation of the major features and subsequent peak broadening at max power. Adjusting the energy available during irradiation, through irradiation time and/or laser power, has a notable impact on spectral features (Figure 5). Irradiation time is more limited in adjustment and does not appear to have as substantial an impact as laser power. As observed for He pressure, both major and minor spectral features are often distinguishable across a wide range of power and irradiation times. This flexibility allows an IRMPD spectrum to be acquired that displays features that are close to the dissociation threshold alongside those that are well above it. Collection of a spectrum under multiple conditions affords the opportunity to either splice spectra together after correcting for the relative energy available for dissociation or create overlays to highlight a feature that may otherwise be difficult to distinguish. An example of this can be seen in Figure 6 where portions of the

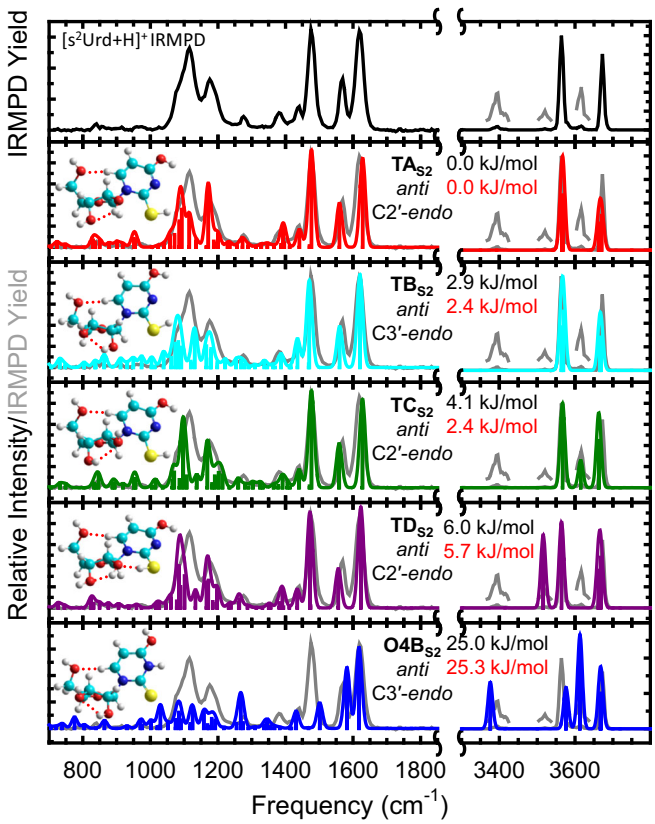

Figure 6. Comparison of the measured IRMPD action spectrum of $[s^2Urd+H]^+$ with the B3LYP/6-311+G(d,p) predicted linear IR spectra for low-energy conformers of $[s^2Urd+H]^+$ that are populated in the experiments. The protonation site, nucleobase orientation, sugar puckering, and relative B3LYP/6-311+G(2d,2p) (black) and MP2/6-311+G(2d,2p) (red) Gibbs free energies at 298 K are indicated. The measured IRMPD action spectrum is superimposed with the calculated spectra and the intensities scaled to facilitate comparisons. Features recollected with greater laser power are overlaid and offset from the baseline to better illustrate these small features

hydrogen-stretching region were also acquired at greater laser power to produce more distinctive features. Choosing appropriate conditions is also critical to feature width, which can have a large impact on the ease of spectral interpretation.

Comparison of Measured IRMPD and Predicted IR Spectra of $[s^2Urd+H]^+$

Representative conformers whose calculated IR spectra exhibit good agreement or exhibit distinctive features are compared to the measured IRMPD spectrum of $[s^2Urd+H]^+$ and shown in Figure 6. Comparisons of representative structures whose computed IR spectra exhibit notable disagreement with the measured spectrum that preclude them from significant population in the experiments are shown in Figures S3, S4, and S5 of the Electronic Supplementary Information. The calculated ground structure **TA_{S2}** provides a good match in relative intensity and peak position for the major features in both the IR fingerprint and hydrogen-stretching regions. **TA_{S2}** displays an *anti* nucleobase orientation with C2′-*endo* sugar puckering. **TB_{S2}** lies within 3 kJ/mol in free energy, is a C3′-*endo*, *anti* conformer, but does not provide the same feature reproduction, particularly in the range of 1000 to 1300 cm^{-1}. These minor differences suggest that while **TB_{S2}** may be present in the experiments, it is likely present at lower abundance that **TA_{S2}**. The shifting of the O3′–H stretch from 3660 cm^{-1} in **TA_{S2}** and **TB_{S2}** to 3611 cm^{-1} in **TC_{S2}** and the reasonable comparison with the IR fingerprint region suggests that **TC_{S2}** conformer may also be present in the experiments. The rotation of the sulfhydryl group in **TD_{S2}**, as seen in Figure 6, allows for formation of a S2H···O2′H···O3′ dual hydrogen bond, and gives a unique spectroscopic signature in the hydrogen-stretching region at 3513 cm^{-1} that is observed in very low intensity, indicating that this structure is likely present in small quantity. Poor matching of spectral features around 1100, 1200, and 1400 cm^{-1}, and the higher relative free energy of the *syn* structures calculated, **TG_{S2}**, **TI_{S2}**, **TJ_{S2}**, **TK_{S2}**, indicates that none of these conformers were present in the experiments.

The absence of a measured feature between 1700 and 1800 cm^{-1} indicates that if any S2 conformers were present in the experiments, which would result in a carbonyl stretch in that range, they must have been present in a very small amount. The most stable O4 and S2 protonated structures, **$O4A_{S2}$** and **$S2A_{S2}$**, are calculated to be at least 20.0 kJ/mol less stable than the calculated ground **TA_{S2}** conformer and their IR spectra lack many major features in the fingerprint region, which would exclude them from the experimental population without further data. However, the measured spectrum in the hydrogen-stretching region is definitive that there must be another conformer present besides sulfhydryl-hydroxyl tautomers to explain the small feature observed at 3390 cm^{-1}, which is a feature not predicted for any of the tautomer spectra calculated. The very small measured features at 3380 and 3608 cm^{-1} that are likely attributed to the **$O4B_{S2}$** conformer also indicate that it is present in the experiment in small abundance. The presence of the **$O4B_{S2}$** conformer would suggest that both B3LYP and MP2 are underestimating the stability of this and other similar O4 protonated conformers.

$[s^2Urd+H]^+$ Conformers Populated by ESI

A mixture of structures of $[s^2Urd+H]^+$ was accessed in the experiments, the dominant structures however were **TA_{S2}** and **TB_{S2}**, C2′-*endo* and C3′-*endo* structures with an *anti* nucleobase orientation that favor individual hydrogen-bonding interactions in the sugar, and between the sugar and nucleobase instead of a dual hydrogen-bonding interaction between the 2-sulfhydryl group and sugar moiety. A small population of **$O4B_{S2}$** must have been present to fully represent the spectrum in the hydrogen-stretching region. The minor tautomers **TC_{S2}**, and **TD_{S2}**, were likely also present in small quantities as indicated by the hydrogen-stretching region. The structures accessed all demonstrate C2′-*endo* or C3′-*endo* sugar puckering with *anti* nucleobase orientations.

Resonant Vibrational Modes of $[s^2Urd+H]^+$

Assignment of vibrational modes in the measured IRMPD spectrum of $[s^2Urd+H]^+$ is based upon the predicted IR spectra of the populated conformers detailed above. The measured bands in the IR fingerprint region are attributed to T conformers. The measured band at 1620 cm^{-1} arises from coupled C2=N3 and C5=C6 stretches, whereas the measured band at 1570 cm^{-1} results from C4–C5 stretching coupled to O4–H bending. The intense band at 1470 cm^{-1} arises from nucleobase ring stretching coupled to C6–H bending. The band at 1180 cm^{-1} is attributed to in-plane bending of O4–H, while the broad band centered at 1115 cm^{-1} arises from stretches of the sugar ring. The band at 3670 cm^{-1} is attributed to O3′–H and O5′–H stretches, while the small band measured at 3614 cm^{-1} may be attributed to O4–H stretching in **$O4B_{S2}$** or O3′–H stretching of **TC_{S2}**. The intense measured band at ~3565 cm^{-1} arises from O4–H and O2′–H stretching of **TA_{S2}**. The small feature measured at ~3395 cm^{-1} arises from N3–H stretching of **$O4B_{S2}$**.

Comparison of Measured IRMPD and Predicted IR Spectra of $[s^4Urd+H]^+$

Predicted linear IR spectra for **$S4A_{S4}$**, **$S4B_{S4}$**, and **TA_{S4}** are compared to the experimental IRMPD spectrum in Figure 7. Other conformers that display either highly parallel spectra to these three conformers, or instead display notable disagreement with the measured spectrum are shown in Figures S6, S7, and S8 of the Electronic Supplementary Information. The calculated IR spectra of the **$S4A_{S4}$**, **$S4B_{S4}$**, and **TA_{S4}** structures are complementary and together exhibit good agreement with the measured IRMPD spectrum. The bands at 3400, 1785, 1575, and 1285 cm^{-1} are not displayed by **TA_{S4}** but compare well with **$S4A_{S4}$** and **$S4B_{S4}$**. The small shoulder measured at 1640 cm^{-1} is attributed solely to the tautomer structures as it is not represented in predicted spectra of S4 conformers and establishes the presence of tautomer conformers in the experiments. The spectra predicted for **$S4A_{S4}$** and **$S4B_{S4}$** reproduce

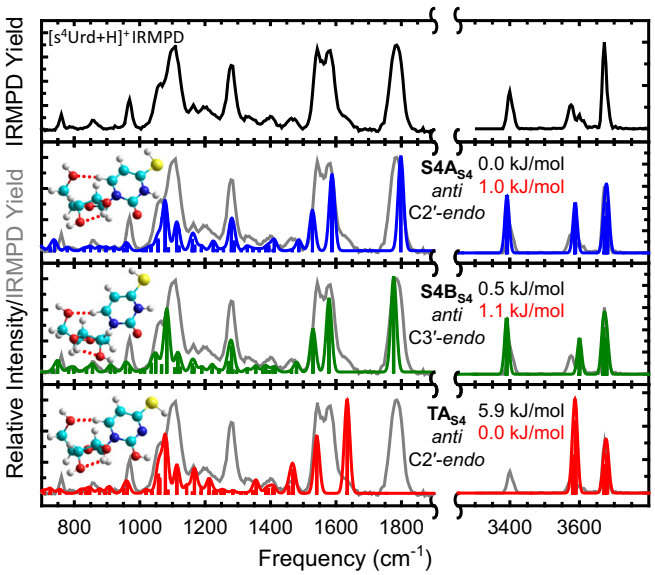

Figure 7. Comparison of the measured IRMPD action spectrum of $[s^4Urd+H]^+$ with the B3LYP/6-311+G(d,p) predicted linear IR spectra for low-energy conformers of $[s^4Urd+H]^+$ that are populated in the experiments. The protonation site, nucleobase orientation, sugar puckering, and relative B3LYP/6-311+G(2d,2p) (black) and MP2/6-311+G(2d,2p) (red) Gibbs free energies at 298 K are indicated. The measured IRMPD action spectrum is superimposed on the calculated spectra and the intensity scaled to facilitate comparisons

the major measured features in both spectral regions well, and the width of the feature at 1785 cm^{-1} likely results from the subtle shifting in position of the C=O stretch between these two conformers. The spectrum predicted for $\mathbf{S4C_{S4}}$ is very parallel to that of $\mathbf{S4A_{S4}}$, whereas the spectrum of $\mathbf{S4E_{S4}}$ is highly parallel to that of $\mathbf{S4B_{S4}}$ with both conformers only marginally higher in free energy and shown in Figure S6. Spectral mismatches for other low-energy conformers compared in Figure S6, often in the low intensity features between 1100 and 1500 cm^{-1}, suggest that they are not populated in the experiment in measurable quantity. The vibrational modes predicted around 3620 cm^{-1} for $\mathbf{S4F_{S4}}$ in the hydrogen-stretching region are misaligned along with greater misalignment with the broad ~1700 to 1800 cm^{-1} band, indicating that while it is calculated to be low in energy by B3LYP and MP2, this conformer is likely not populated in the experiments. $\mathbf{TE_{S4}}$, the most stable *syn* conformer computed, exhibits disagreement in both the fingerprint and hydrogen-stretching regions precluding it from a discernible population in the experiment. The switching of the calculated ground conformer from $\mathbf{S4A_{S4}}$ to $\mathbf{TA_{S4}}$ for B3LYP vs. MP2 and the relative intensities of the peaks differentiating S4 and T conformers suggests that B3LYP does a better job predicting relative energetics for this system.

$[s^4Urd+H]^+$ Conformers Populated by ESI

A mixture of the low-energy S4 conformers $\mathbf{S4A_{S4}}$, $\mathbf{S4B_{S4}}$, $\mathbf{S4C_{S4}}$, and $\mathbf{S4E_{S4}}$ is present in the experiments; also present is the low-energy $\mathbf{TA_{S4}}$ conformer. $\mathbf{S4A_{S4}}$, $\mathbf{S4C_{S4}}$, and $\mathbf{TA_{S4}}$ exhibit C2′-*endo* sugar puckering, whereas $\mathbf{S4B_{S4}}$ and $\mathbf{S4E_{S4}}$ exhibit C3′-*endo* puckering and all five conformers display *anti* nucleobase orientations. The major difference between $\mathbf{S4A_{S4}}$ and $\mathbf{S4C_{S4}}$ as well as $\mathbf{S4B_{S4}}$ and $\mathbf{S4E_{S4}}$ is the rotation of the 4-sulfhydryl moiety, which results in both minimal changes to the predicted spectra and only small shifts in relative stability calculated by both B3LYP and MP2. No structures displaying a *syn* nucleobase contribute to the experiments.

Resonant Vibrational Modes of $[s^4Urd+H]^+$

Features in the measured IRMPD spectrum of $[s^4Urd+H]^+$ are assigned to vibrational modes based on the conformations found to be populated in the experiments. In the IR fingerprint region, the measured band at 1790 cm^{-1} arises from the C2=O stretches of the S4 conformers, $\mathbf{S4A_{S4}}$ and $\mathbf{S4B_{S4}}$, resulting in the observed broad feature. The measured shoulder at 1640 cm^{-1} arises from the coupled C2=N3 and C5=C6 stretches of $\mathbf{TA_{S4}}$. The intense feature at 1580 cm^{-1} is attributed to C5=C6 stretching of S4 conformers and the nearby feature at 1545 cm^{-1} arises from C4–C5 stretching of S4 and T_{S4} structures. The band at 1285 cm^{-1} can be attributed to nucleobase ring stretching coupled to S4–H bending of the S4 structures. The broad band at 1110 cm^{-1} represents stretches of the sugar ring. The intense feature in the hydrogen-stretching region at 3670 cm^{-1} represents O3′–H and O5′–H stretches. The broader feature around 3575 cm^{-1} arises from the O2′–H stretches of S4 and T conformers and the O2–H stretching of the tautomers.

Comparison to IRMPD and Theoretical Studies of Protonated Thiouracils

The measured IRMPD spectra of the protonated forms of the 2-thiouracil and 4-thiouracil nucleobases, $[s^2Ura+H]^+$ and $[s^4Ura+H]^+$ [58], in the IR fingerprint region are compared with their nucleoside counterparts in Figure 8. There are notable parallels between these spectra, most evident in the range of 1400–1900 cm^{-1}, a region largely attributed to the vibrational modes of the nucleobase. Relative peak positions are reasonably well reproduced between the analogous nucleoside and nucleobase with some minor shifting. The measured features are much more intense and broad in the nucleobase spectrum and have been scaled down to facilitate comparison. A previous study identified the preferred protonation state of $[s^2Ura+H]^+$ as the minor T tautomer, with the most stable O4 protonated conformer lying 20.5 kJ/mol higher in free energy. Although the IR spectrum predicted for this conformer matched much of the measured $[s^2Ura+H]^+$ spectrum reasonably well with one small feature not well represented, it was concluded that this conformer was not populated in the IR fingerprint experiment. Analysis of the IR fingerprint spectrum of $[s^2Urd+H]^+$ would suggest that this conclusion is also valid for the nucleoside; however, the addition of spectral information in the hydrogen-stretching region provides clear evidence for a small population of an O4 species. The IR fingerprint region spectrum of $[s^4Ura+H]^+$ is best represented by S4 protonated

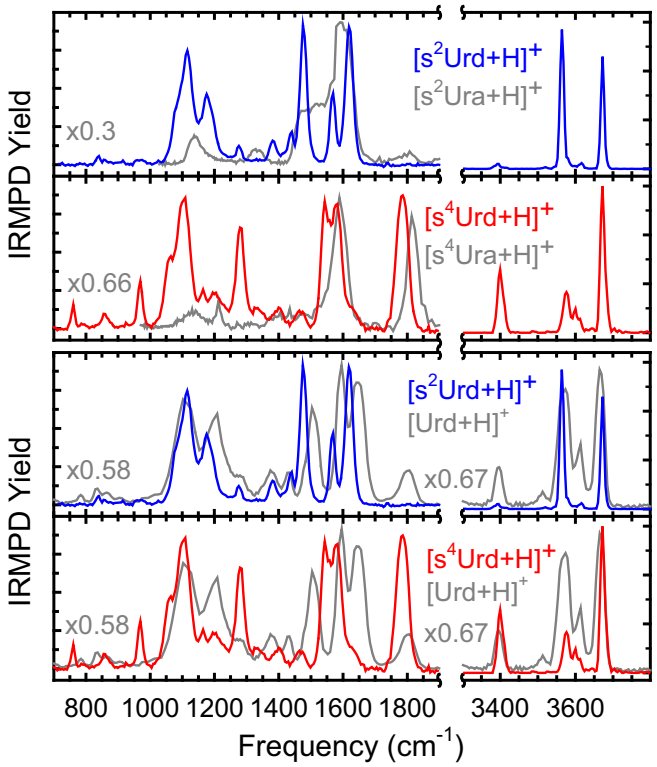

Figure 8. Comparison of experimental IRMPD spectra of $[s^2Urd+H]^+$ and $[s^4Urd+H]^+$ in both the IR fingerprint and hydrogen-stretching regions with spectra in the IR fingerprint region for the corresponding protonated nucleobases, $[s^2Ura+H]^+$ and $[s^4Ura+H]^+$, taken from Reference [55], and over both regions for the protonated canonical nucleoside, $[Urd+H]^+$, taken from Reference [24]

conformers, but the most stable T tautomers exhibit many features similar to the measured spectra and are calculated to be only 3.0 kJ/mol less stable. This agrees well with the energetics and spectral comparisons of $[s^4Urd+H]^+$, which displays more distinctive differences between the O4 protonated and T spectra, particularly in the IR fingerprint region where the shoulder attributed to the tautomer is better resolved.

Comparison to IRMPD and Theoretical Studies of Protonated Canonical Uridine

The spectrum of $[Urd+H]^+$ [27] is compared with those measured for $[s^2Urd+H]^+$ and $[s^4Urd+H]^+$ in Figure 8. Many of the major features are highly parallel, with the notable exception being the red shifting of many nucleobase ring stretching modes of the thiouridines. The structures of these features are largely preserved however, and major differences beyond this are attributed to changes in the protonation preferences as compared to the more competitive mixture of O4 and T conformers found for $[Urd+H]^+$. Differences in the relative intensities of the features measured for $[s^2Urd+H]^+$ between ~1400 and 1700 cm^{-1}, as well as the hydrogen-stretching feature at ~3380 cm^{-1}, can be attributed to a decrease in the importance of the O4 conformer versus $[Urd+H]^+$, which was largely populated by T conformers. The much larger relative intensity of the carbonyl stretch at ~1785 cm^{-1} in $[s^4Urd+H]^+$ versus $[Urd+H]^+$ also reflects the change in protonation preference shifting towards S4 protonation, alongside a related decrease in the relative intensity of the features at ~1466 cm^{-1}. The sugars in all three systems exhibit a mixture of C2′-*endo* and C3′-*endo* puckering with difficulty in differentiating these features spectroscopically. A *syn* tautomer structure involving rotation of the substituent at the 2-position to hydrogen bond with O5′ was found relatively low in free energy for $[Urd+H]^+$, but it is not favorable spectroscopically or energetically for either protonated thiouridine.

Comparison of $[s^2Urd+H]^+$ to Studies of Neutral 2-Thiouridine

Previous studies of neutral 2-thiouridine by NMR [42, 44, 45], crystallography [43], and electronic structure calculations [73, 74] all indicate a preference for C3′-*endo* sugar puckering. Structure characterization by NMR has shown that uridine has a 0.4 kJ/mol preference for C3′-*endo* over C2′-*endo*, while 2-thiouridine enhances that stabilization to 4.2 kJ/mol. This preference was also found in a crystallography study in which a C3′-*endo*, *anti* structure was found. The consensus of these studies was that thiation has little effect on the conformational parameters, with only minor stabilization of C3′-*endo* sugar puckering. Parallel to this in the gas phase, the largest differences in conformational parameters between $[Urd+H]^+$ and $[s^2Urd+H]^+$ are a result of protonation, with sugar puckering and nucleobase orientation remaining largely consistent. However, the lack of spectroscopic distinction between C2′-*endo* and C3′-*endo* puckering combined with calculated energetics that place the two sugar puckering modes very close in energy, cannot definitively confirm a preference for C3′-*endo* puckering in the protonated gas-phase species.

Conclusions

The hydrogen-stretching region is of great utility in the analysis of structure by ion spectroscopy, and the instrument described here will be a valuable asset for structural characterization. A commercial QIT MS was modified and coupled with a tunable OPO laser system for acquisition of IRMPD action spectra in the hydrogen-stretching region. This instrument was then used to collect IRMPD action spectra for two protonated thiated uridines, $[s^2Urd+H]^+$ and $[s^4Urd+H]^+$. Complementary spectra were collected in the IR fingerprint region using a FEL. Synergistic calculations were used to generate candidate structures and predict their linear IR spectra. Comparisons between predicted IR spectra and measured IRMPD spectra determined the conformers populated by ESI. Mixtures of 4-protonated and hydroxyl-sulfhydryl or sulfhydryl-hydroxyl tautomer structures are found experimentally for these thiouridines. $[s^2Urd+H]^+$ displays a strong preference for the T structures, whereas $[s^4Urd+H]^+$ demonstrates a preference for S4 protonation. Structures exhibiting a mixture of C2′-*endo* and C3′-*endo* sugar puckering and only *anti* nucleobase orientations were populated in the experiments for both species.

Acknowledgments

This work was financially supported by the National Science Foundation, Grants OISE-0730072 and OISE-1357887 (for the FEL IRMPD measurements and international travel), and DBI-0922819 (for the Bruker amaZon ETD QITMS), and CHE-1709789 (for other research costs). This work is part of the research program of FOM, which is financially supported by the Nederlandse Organisatie voor Wetenschappeklijk Onderzoek (NWO). The authors acknowledge WSU C&IT for the exemplary computational resources and support provided. L.A.H., Y.Z., and Z.J.D. gratefully acknowledge support from the Wayne State University Thomas C. Rumble Graduate Fellowships. Z.J.D. also acknowledges support from the Joseph Jasper Scholarship for Graduate Students in Chemistry. The authors gratefully acknowledge extraordinarily helpful conversations with Dr. J. Martens and Dr. G. Berden regarding the hardware and software modifications. Their assistance alongside Dr. J. Oomens and the rest of the FELIX staff in the use of the FEL involved in this work is greatly appreciated. The assistance of Christoph R. Gebhardt at Bruker in the establishment of software synchronization is gratefully appreciated.

References

1. Fridgen, T.D.: Infrared consequence spectroscopy of gaseous protonated and metal ion cationized complexes. Mass Spectrom. Rev. **28**, 586–607 (2009)
2. Bush, M.F., O'Brien, J.T., Prell, J.S., Saykally, R.J., Williams, E.R.: Infrared spectroscopy of cationized arginine in the gas phase: direct evidence for the transition from nonzwitterionic to zwitterionic structure. J. Am. Chem. Soc. **129**, 1612–1622 (2007)
3. MacAleese, L., Maitre, P.: Infrared spectroscopy of organometallic ions in the gas phase: from model to real world complexes. Mass Spectrom. Rev. **26**, 583–605 (2007)
4. Stedwell, C.N., Galindo, J.F., Roitberg, A.E., Polfer, N.C.: Structures of biomolecular ions in the gas phase probed by infrared light sources. Annu. Rev. Anal. Chem. **6**, 267–285 (2013)
5. Miyamoto, Y., Majima, T., Arai, S., Katsumata, K., Akagi, H., Maeda, A., Hata, H., Kuramochi, K., Kato, Y., Tsukiyama, K.: ^{13}C-selective infrared multiple photon dissociation of beta-propiolactone by a free electron laser. Nucl. Instrum. Methods Phys. Res. Sect. B. **269**, 180–184 (2011)
6. Valle, J.J., Eyler, J.R., Oomens, J., Moore, D.T., van der Meer, A.F.G., von Helden, G., Meijer, G., Hendrickson, C.L., Marshall, A.G., Blakney, G.T.: Free electron laser-Fourier transform ion cyclotron resonance mass spectrometry facility for obtaining infrared multiphoton dissociation spectra of gaseous ions. Rev. Sci. Instrum. **76**, 023103–023107 (2005)
7. Hoffmann, W., Marianski, M., Warnke, S., Seo, J., Baldauf, C., von Helden, G., Pagel, K.: Assessing the stability of alanine-based helices by conformer-selective IR spectroscopy. Phys. Chem. Chem. Phys. **18**, 19950–19954 (2016)
8. Lemaire, J., Boissel, P., Heninger, M., Mauclaire, G., Bellec, G., Mestdagh, H., Simon, A., Caer, S.L., Ortega, J.M., Glotin, F., Maitre, P.: Gas phase infrared spectroscopy of selectively prepared ions. Phys. Rev. Lett. **89**, 273002 (2002)
9. Polfer, N.C.: Infrared multiple photon dissociation spectroscopy of trapped ions. Chem. Soc. Rev. **40**, 2211–2221 (2011)
10. Avilés-Moreno, J.R., Berden, G., Oomens, J., Martínez-Haya, B.: Intracavity proton bonding and anharmonicity in the anionophore cyclen. Phys. Chem. Chem. Phys. **20**, 8968–8975 (2018)
11. Jos, O., Giel, B., Hellman, M.T.: Low-frequency CH stretch vibrations of free alkoxide ions. Angew. Chem. **129**, 223–226 (2017)
12. Wolk, A.B., Leavitt, C.M., Garand, E., Johnson, M.A.: Cryogenic ion chemistry and spectroscopy. Acc. Chem. Res. **47**, 202–210 (2014)
13. Asvany, O., Brunken, S., Kluge, L., Schlemmer, S.: COLTRAP: a 22-pole ion trapping machine for spectroscopy at 4 K. Appl. Phys. B Lasers Opt. **114**, 203–211 (2014)
14. Jasik, J., Zabka, J., Roithova, J., Gerlich, D.: Infrared spectroscopy of trapped molecular dications below 4 K. Int. J. Mass Spectrom. **354**, 204–210 (2013)
15. Kamrath, M.Z., Relph, R.A., Guasco, T.L., Leavitt, C.M., Johnson, M.A.: Vibrational predissociation spectroscopy of the H_2 tagged mono- and dicarboxylate anions of dodecanedioic acid. Int. J. Mass Spectrom. **300**, 91–98 (2011)
16. Redwine, J.G., Davis, Z.A., Burke, N.L., Oglesbee, R.A., McLuckey, S.A., Zwier, T.S.: A novel ion trap based tandem mass spectrometer for the spectroscopic study of cold gas phase polyatomic ions. Int. J. Mass Spectrom. **348**, 9–14 (2013)
17. Remes, P.A., Glish, G.L.: Collisional cooling in a quadrupole ion trap at sub-ambient temperatures. Int. J. Mass Spectrom. **265**, 176–181 (2007)
18. Heine, N., Fagiani, M.R., Rossi, M., Wende, T., Berden, G., Blum, V., Asmis, K.R.: Isomer-selective detection of hydrogen-bond vibrations in the protonated water hexamer. J. Am. Chem. Soc. **135**, 8266–8273 (2013)
19. Eyler, J.R.: Infrared multiple photon dissociation spectroscopy of ions in penning traps. Mass Spectrom. Rev. **28**, 448–467 (2009)
20. Mauclaire, G., Lemaire, J., Boissel, P., Bellec, G., Heninger, M.: MICRA: a compact permanent magnet Fourier transform ion cyclotron resonance mass spectrometer. Eur. J. Mass Spectrom. **10**, 155–162 (2004)
21. Oomens, J., van Roij, A.J.A., Meijer, G., von Helden, G.: Gas-phase infrared photodissociation spectroscopy of cationic polyaromatic hydrocarbons. Astrophys. J. **542**, 404–410 (2000)
22. Newsome, G.A., Glish, G.L.: Improving IRMPD in a quadrupole ion trap. J. Am. Soc. Mass Spectrom. **20**, 1127–1131 (2009)
23. Gulyuz, K., Stedwell, C.N., Wang, D., Polfer, N.C.: Hybrid quadrupole mass filter/quadrupole ion trap time-of-flight-mass spectrometer for infrared multiple photon dissociation spectroscopy of mass-selected ions. Rev. Sci. Instrum. **82**, 054101–054107 (2011)
24. Martens, J., Berden, G., Gebhardt, C.R., Oomens, J.: Infrared ion spectroscopy in a modified quadrupole ion trap mass spectrometer at the FELIX free electron laser laboratory. Rev. Sci. Instrum. **87**, 103108–103108 (2016)
25. Wu, R.R., He, C.C., Hamlow, L.A., Nei, Y.-W., Berden, G., Oomens, J., Rodgers, M.T.: N3 protonation induces base rotation of 2′-deoxyadenosine-5′-monophosphate and adenosine-5′-monophosphate. J. Phys. Chem. B. **120**, 4616–4624 (2016)
26. Wu, R.R., Yang, B., Frieler, C.E., Berden, G., Oomens, J., Rodgers, M.T.: 2,4-Dihydroxy and O_2 protonated tautomers of dThd and Thd coexist in the gas phase: methylation alters protonation preferences versus dUrd and Urd. J. Am. Soc. Mass Spectrom. **27**, 410–421 (2016)
27. Wu, R.R., Yang, B., Frieler, C.E., Berden, G., Oomens, J., Rodgers, M.T.: Diverse mixtures of 2,4-dihydroxy tautomers and O4 protonated conformers of uridine and 2′-deoxyuridine coexist in the gas phase. Phys. Chem. Chem. Phys. **17**, 25978–25988 (2015)
28. Zhu, Y., Hamlow, L.A., He, C.C., Strobehn, S.F., Lee, J.K., Gao, J., Berden, G., Oomens, J., Rodgers, M.T.: Influence of sodium cationization versus protonation on the gas-phase conformations and glycosidic bond stabilities of 2′-deoxyadenosine and adenosine. J. Phys. Chem. B. **120**, 8892–8904 (2016)
29. Zhu, Y., Hamlow, L.A., He, C.C., Lee, J.K., Gao, J., Berden, G., Oomens, J., Rodgers, M.T.: Gas-phase conformations and N-glycosidic bond stabilities of sodium cationized 2′-deoxyguanosine and guanosine: sodium cations preferentially bind to the guanine residue. J. Phys. Chem. B. **121**, 4048–4060 (2017)
30. Wu, R.R., Yang, B., Berden, G., Oomens, J., Rodgers, M.T.: Gas-phase conformations and energetics of protonated 2′-deoxyguanosine and guanosine: IRMPD action spectroscopy and theoretical studies. J. Phys. Chem. B. **118**, 14774–14784 (2014)
31. Wu, R.R., Yang, B., Berden, G., Oomens, J., Rodgers, M.T.: Gas-phase conformations and energetics of protonated 2′-deoxyadenosine and adenosine: IRMPD action spectroscopy and theoretical studies. J. Phys. Chem. B. **119**, 2795–2805 (2015)
32. Wu, R.R., Yang, B., Frieler, C.E., Berden, G., Oomens, J., Rodgers, M.T.: N3 and O2 protonated tautomeric conformations of 2′-deoxycytidine and cytidine coexist in the gas phase. J. Phys. Chem. B. **119**, 5773–5784 (2015)
33. Zhu, Y., Roy, H.A., Cunningham, N.A., Strobehn, S.F., Gao, J., Munshi, M.U., Berden, G., Oomens, J., Rodgers, M.: Effects of sodium cationization versus protonation on the conformations and N-glycosidic bond stabilities of sodium cationized uridine and 2′-deoxyuridine: solution conformation of $[Urd+Na]^+$ is preserved upon ESI. Phys. Chem. Chem. Phys. **19**, 17637–17652 (2017)

34. Zhu, Y., Hamlow, L., He, C., Roy, H., Cunningham, N., Munshi, M., Berden, G., Oomens, J., Rodgers, M.: Conformations and N-glycosidic bond stabilities of sodium cationized 2′-deoxycytidine and cytidine: solution conformation of $[Cyd+Na]^+$ is preserved upon ESI. Int. J. Mass Spectrom. **429**, 18–27 (2018)
35. Zhu, Y., Roy, H.A., Cunningham, N.A., Strobehn, S.F., Gao, J., Munshi, M.U., Berden, G., Oomens, J., Rodgers, M.T.: IRMPD action spectroscopy, ER-CID experiments, and theoretical studies of sodium cationized thymidine and 5-methyluridine: kinetic trapping during the ESI desolvation process preserves the solution structure of $[Thd+Na]^+$. J. Am. Soc. Mass Spectrom. **28**, 2423–2437 (2017)
36. Yarian, C., Townsend, H., Czestkowski, W., Sochacka, E., Malkiewicz, A.J., Guenther, R., Miskiewicz, A., Agris, P.F.: Accurate translation of the genetic code depends on tRNA modified nucleosides. J. Biol. Chem. **277**, 16391–16395 (2002)
37. Agris, P.F., Vendeix, F.A.P., Graham, W.D.: tRNA's wobble decoding of the genome: 40 years of modification. J. Mol. Biol. **366**, 1–13 (2007)
38. Crick, F.H.C.: Codon-anticodon pairing—wobble hypothesis. J. Mol. Biol. **19**, 548–555 (1966)
39. Agris, P.F.: Wobble position modified nucleosides evolved to select transfer-RNA codon recognition—a modified-wobble hypothesis. Biochimie. **73**, 1345–1349 (1991)
40. McCloskey, J.A., Nishimura, S.: Modified nucleosides in transfer-RNA. Acc. Chem. Res. **10**, 403–410 (1977)
41. Grosjean, H.J., Dehenau, S., Crothers, D.M.: Physical basis for ambiguity in genetic coding interactions. Proc. Natl. Acad. Sci. U. S. A. **75**, 610–614 (1978)
42. Smith, W.S., Sierzputowskagracz, H., Sochacka, E., Malkiewicz, A., Agris, P.F.: Chemistry and structure of modified uridine dinucleosides are determined by thiolation. J. Am. Chem. Soc. **114**, 7989–7997 (1992)
43. Hawkinson, S.W.: Crystal and molecular-structure of 2-thiouridine. Acta Crystallogr. B. **33**, 80–85 (1977)
44. Yokoyama, S., Watanabe, T., Murao, K., Ishikura, H., Yamaizumi, Z., Nishimura, S., Miyazawa, T.: Molecular mechanism of codon recognition by transfer-RNA species with modified uridine in the 1st position of the anticodon. Proc. Natl. Acad. Sci. U. S. A. **82**, 4905–4909 (1985)
45. Agris, P.F., Sierzputowskagracz, H., Smith, W., Malkiewicz, A., Sochacka, E., Nawrot, B.: Thiolation of uridine carbon-2 restricts the motional dynamics of the transfer-RNA wobble position nucleoside. J. Am. Chem. Soc. **114**, 2652–2656 (1992)
46. Kumar, R.K., Davis, D.R.: Synthesis and studies on the effect of 2-thiouridine and 4-thiouridine on sugar conformation and RNA duplex stability. Nucleic Acids Res. **25**, 1272–1280 (1997)
47. Ashraf, S.S., Sochacka, E., Cain, R., Guenther, R., Malkiewicz, A., Agris, P.F.: Single atom modification (O → S) of tRNA confers ribosome binding. RNA. **5**, 188–194 (1999)
48. Fourrey, J.L., Gasche, J., Fontaine, C., Guittet, E., Favre, A.: Sequence dependent photochemistry of di(deoxynucleoside) phosphates containing 4-thiouracil. J. Chem. Soc. Chem. Commun. **18**, 1334–1336 (1989)
49. Mueller, E.G., Buck, C.J., Palenchar, P.M., Barnhart, L.E., Paulson, J.L.: Identification of a gene involved in the generation of 4-thiouridine in tRNA. Nucleic Acids Res. **26**, 2606–2610 (1998)
50. Khvorostov, A., Lapinski, L., Rostkowska, H., Nowak, M.J.: Unimolecular photochemistry of 4-thiouracils. Photochem. Photobiol. **81**, 1205–1211 (2005)
51. Thomas, G., Favre, A.: 4-Thiouridine triggers both growth delay induced by near-ultraviolet light and photoprotection. Eur. J. Biochem. **113**, 67–74 (1980)
52. Spitzer, J., Hafner, M., Landthaler, M., Ascano, M., Farazi, T., Wardle, G., Nusbaum, J., Khorshid, M., Burger, L., Zavolan, M., Tuschl, T.: PAR-CLIP (photoactivatable ribonucleoside-enhanced crosslinking and immunoprecipitation): a step-by-step protocol to the transcriptome-wide identification of binding sites of RNA-binding proteins. Methods Enzymol. **539**, 113–161 (2014)
53. Rabani, M., Levin, J.Z., Fan, L., Adiconis, X., Raychowdhury, R., Garber, M., Gnirke, A., Nusbaum, C., Hacohen, N., Friedman, N., Amit, I., Regev, A.: Metabolic labeling of RNA uncovers principles of RNA production and degradation dynamics in mammalian cells. Nat. Biotechnol. **29**, 436–442 (2011)
54. Kramer, K., Sachsenberg, T., Beckmann, B.M., Qamar, S., Boon, K.L., Hentze, M.W., Kohlbacher, O., Urlaub, H.: Photo-cross-linking and high-resolution mass spectrometry for assignment of RNA-binding sites in RNA-binding proteins. Nat. Methods. **11**, 1064–1070 (2014)
55. Su, D., Chan, C.T.Y., Gu, C., Lim, K.S., Chionh, Y.H., McBee, M.E., Russell, B.S., Babu, I.R., Begley, T.J., Dedon, P.C.: Quantitative analysis of ribonucleoside modifications in tRNA by HPLC-coupled mass spectrometry. Nat. Protoc. **9**, 828–841 (2014)
56. Scheibe, M., Butter, F., Hafner, M., Tuschl, T., Mann, M.: Quantitative mass spectrometry and PAR-CLIP to identify RNA-protein interactions. Nucleic Acids Res. **40**, 9897–9902 (2012)
57. Gaston, K.W., Limbach, P.A.: The identification and characterization of non-coding and coding RNAs and their modified nucleosides by mass spectrometry. RNA Biol. **11**, 1568–1585 (2014)
58. Nei, Y.-W., Akinyemi, T.E., Steill, J.D., Oomens, J., Rodgers, M.T.: Infrared multiple photon dissociation action spectroscopy of protonated uracil and thiouracils: effects of thioketo-substitution on gas-phase conformation. Int. J. Mass Spectrom. **297**, 139–151 (2010)
59. Polfer, N.C., Oomens, J., Moore, D.T., von Helden, G., Meijer, G., Dunbar, R.C.: Infrared spectroscopy of phenylalanine ag(I) and Zn(II) complexes in the gas phase. J. Am. Chem. Soc. **128**, 517–525 (2006)
60. Polfer, N.C., Oomens, J.: Reaction products in mass spectrometry elucidated with infrared spectroscopy. Phys. Chem. Chem. Phys. **9**, 3804–3817 (2007)
61. Oepts, D., Vandermeer, A.F.G., Vanamersfoort, P.W.: The free-electron-laser user facility FELIX. Infrared Phys. Technol. **36**, 297–308 (1995)
62. Frisch, M.J., Trucks, G.W., Schlegel, H.B., Scuseria, G.E., Robb, M.A., Cheeseman, J.R., Scalmani, G., Barone, V., Mennucci, B., Petersson, G.A., Nakatsuji, H., Caricato, M., Li, X., Hratchian, H.P., Izmaylov, A.F., Bloino, J., Zheng, G., Sonnenberg, J.L., Hada, M., Ehara, M., Toyota, K., Fukuda, R., Hasegawa, J., Ishida, M., Nakajima, T., Honda, Y., Kitao, O., Nakai, H., Vreven, T., Montgomery Jr., J.A., Peralta, J.E., Ogliaro, F., Bearpark, M.J., Heyd, J., Brothers, E.N., Kudin, K.N., Staroverov, V.N., Kobayashi, R., Normand, J., Raghavachari, K., Rendell, A.P., Burant, J.C., Iyengar, S.S., Tomasi, J., Cossi, M., Rega, N., Millam, N.J., Klene, M., Knox, J.E., Cross, J.B., Bakken, V., Adamo, C., Jaramillo, J., Gomperts, R., Stratmann, R.E., Yazyev, O., Austin, A.J., Cammi, R., Pomelli, C., Ochterski, J.W., Martin, R.L., Morokuma, K., Zakrzewski, V.G., Voth, G.A., Salvador, P., Dannenberg, J.J., Dapprich, S., Daniels, A.D., Farkas, Ö., Foresman, J.B., Ortiz, J.V., Cioslowski, J., Fox, D.J.: Gaussian 09. Gaussian, Inc., Wallingford, CT (2009)
63. Kempkes, L.J.M., Boles, G.C., Martens, J., Berden, G., Armentrout, P.B., Oomens, J.: Deamidation of protonated asparagine–valine investigated by a combined spectroscopic, guided ion beam, and theoretical study. J. Phys. Chem. A. **122**, 2424–2436 (2018)
64. Wu, R., Rodgers, M.: Mechanisms and energetics for N-glycosidic bond cleavage of protonated adenine nucleosides: N3 protonation induces base rotation and enhances N-glycosidic bond stability. Phys. Chem. Chem. Phys. **18**, 16021–16032 (2016)
65. Wu, R., Rodgers, M.: O2 protonation controls threshold behavior for N-glycosidic bond cleavage of protonated cytosine nucleosides. J. Phys. Chem. B. **120**, 4803–4811 (2016)
66. Wu, R., Chen, Y., Rodgers, M.: Mechanisms and energetics for N-glycosidic bond cleavage of protonated 2′-deoxyguanosine and guanosine. Phys. Chem. Chem. Phys. **18**, 2968–2980 (2016)
67. Wu, R., Rodgers, M.: Tautomerization lowers the activation barriers for N-glycosidic bond cleavage of protonated uridine and 2′-deoxyuridine. Phys. Chem. Chem. Phys. **18**, 24451–24459 (2016)
68. Boles, G.C., Wu, R.R., Rodgers, M.T., Armentrout, P.B.: Thermodynamics and mechanisms of protonated asparaginyl-glycine decomposition. J. Phys. Chem. B. **120**, 6525–6545 (2016)
69. Mookherjee, A., Van Stipdonk, M.J., Armentrout, P.B.: Thermodynamics and reaction mechanisms of decomposition of the simplest protonated tripeptide, triglycine: a guided ion beam and computational study. J. Am. Soc. Mass. Spectrom. **28**, 739–757 (2017)
70. Mino, W.K., Gulyuz, K., Wang, D., Stedwell, C.N., Polfer, N.C.: Gas-phase structure and dissociation chemistry of protonated tryptophan elucidated by infrared multiple-photon dissociation spectroscopy. J. Phys. Chem. Lett. **2**, 299–304 (2011)
71. Altona, C., Sundaralingam, M.: Conformational-analysis of sugar ring in nucleosides and nucleotides—new description using concept of pseudorotation. J. Am. Chem. Soc. **94**, 8205–8212 (1972)
72. Hoogsteen, K.: The crystal and molecular structure of a hydrogen-bonded complex between 1-methylthymine and 9-methyladenine. Acta Cryst. **16**, 907–916 (1963)
73. Shukla, M.K., Leszczynski, J.: Electronic transitions of thiouracils in the gas phase and in solutions: time-dependent density functional theory (TD-DFT) study. J. Phys. Chem. A. **108**, 10367–10375 (2004)
74. Zhang, R.B., Eriksson, L.A.: Theoretical study on conformational preferences of ribose in 2-thiouridine—the role of the 2' OH group. Phys. Chem. Chem. Phys. **12**, 3690–3697 (2010)